Heavy sterile neutrinos in stellar core-collapse

T. Rembiasz,[1] M. Obergaulinger,[1] M. Masip,[2] M. A. Pérez-García,[3] M. A. Aloy,[1] and C. Albertus[3]
[1]*Departamento de Astronomía y Astrofísica, Universidad de Valencia, C/ Dr. Moliner 50, E-46100 Burjassot, Spain*
[2]*CAFPE and Departamento de Física Teórica y del Cosmos, Universidad de Granada, E-18071, Spain*
[3]*Department of Fundamental Physics, University of Salamanca, Plaza de la Merced s/n E-37008, Spain*

(Received 31 May 2018; published 12 November 2018)

We perform spherically symmetric simulations of the core collapse of a single progenitor star of zero age main sequence mass $M_{\mathrm{ZAMS}} = 15\ M_\odot$ with two models of heavy sterile neutrinos in the mass range of 100 MeV$/c^2$. According to both models, these hypothetical particles are copiously produced in the center, stream outwards and subsequently decay, releasing energy into final states (including neutrinos) of the Standard Model. We find that they can lead to a successful explosion in otherwise nonexploding progenitors. Depending on their unknown parameters (e.g., mass and coupling constants with matter), we obtain either no explosion or an explosion of one of two types, i.e., through heating of gas downstream of the stalled shock wave, similar to the standard scenario for supernova explosions, or through heating of gas at higher radii that ejects matter from the outer core or the envelope while the center continues to accrete matter. In both cases, the explosion energies can be very high. We presume that this new type of explosion would produce an electromagnetic signal that significantly differs from common events because of the relative absence of heavy elements in the ejecta. The combination of core-collapse simulations and astrophysical observations may further constrain the parameters of the sterile neutrinos.

DOI: 10.1103/PhysRevD.98.103010

I. INTRODUCTION

Although neutrinos are a fundamental ingredient of the Standard Model (SM), it has only been during the last decades that detectors have reached the sensitivity and statistics required to study their properties. Today, we have a basic scheme of mass differences and mixings among the three flavors that provides a good fit to the data, but some fundamental questions concerning their absolute mass and hierarchy, their Dirac or Majorana nature, or even the existence of additional sterile modes remain unanswered. In particular, the presence of some persistent anomalies in reactor [1], gallium [2], and baseline [3–5] experiments underlines the possibility of a nonminimal neutrino sector [6].

Despite their weak couplings, cosmology and astrophysics probe the properties of neutrinos in a variety of energy ranges. In the early universe, neutrinos were in thermal equilibrium with matter at the temperature $T > 1\ \mathrm{MeV}/k_{\mathrm{B}} \approx 10^{10}\ \mathrm{K}$,[1] whereas in stars like the Sun, they are copiously produced through nuclear reactions. Proto-neutron stars (PNSs) formed during the core-collapse previous to a supernova explosion are another testing ground for the physics in this sector. During a 10–20 s period, they reach large densities and temperatures exceeding $\sim 30\ \mathrm{MeV}/k_{\mathrm{B}}$, and their long-term evolution is also sensitive to the presence of any long-lived exotic particles with sub-GeV$/c^2$ mass [7–10]. In general, to avoid experimental bounds, the coupling of these hypothetical particles to matter must be very weak. This implies that, if produced in a PNS, they tend to escape faster than standard neutrinos, adding a source of energy loss that shortens the cooling time and the duration of the neutrino signal from a supernova explosion. That argument has been used to set stringent limits on models with axions, sterile neutrinos or Kaluza-Klein excitations of the graviton [11].

On the other hand, current simulations of supernova explosions seem to face a generic difficulty. Once the core exhausts all the nuclear fuel and collapses, most simulations predict the appearance of a stalled shock-front at a few hundred km from the core. A successful supernova explosion requires then that a significant fraction of the energy in the PNS be transferred to the gas behind the shock-front. The current standard supernova model is based on the fact that (active) neutrinos streaming out of the PNS deposit energy in the semitransparent postshock layer. Simulations show that neutrino heating alone does not suffice to revive the stalled shock in most stars. Several of these cases produce an explosion if the efficiency of heating is

[1]We use Heaviside-Lorentz units with explicitly written c, $\hbar$, and k_{B} (the speed of light, the reduced Planck constant, and the Boltzmann constant, respectively).

enhanced by nonspherical flows. Currently, open problems include the conditions for triggering an explosion by this mechanism, the range of explosion energies and ejecta masses that can be achieved, and whether or not previous successes from axisymmetric modeling can be reproduced by the recently started, computationally much more demanding three-dimensional simulations (for a review, see, e.g., [12,13]). Other mechanisms such as magneto-rotational explosions have been considered [14,15]. However, in contrast to neutrino heating, which prevails in any postcollapse core, they rely on conditions (i.e., rapid rotation or strong magnetic fields) that only are present in a small class of progenitors.

A parallel line of research considers the potential of variations of the input from nuclear and particle physics to resolve these open questions. Some of these variations involve effects that are confirmed by particle physics, but whose uncertainties or numerical complexities so far prevented their implementation in supernova simulations, like the production of muons [16] or neutrino flavor oscillations (for a review, see [17]). Others explore more speculative modifications to the standard microphysics such as the phase transition to quark matter at high densities, which is capable of producing explosions even in spherical symmetry [18].

In this context, sterile neutrinos [19] are another interesting possibility. These neutrinos are SM singlets with neither gauge nor Yukawa interactions with standard quarks and leptons. However, as we detail in the next section, they may couple to matter through mixing with the active neutrinos or through one-loop diagrams involving charged particles in the TeV$/c^2$ mass range. Sterile neutrinos in the keV$/c^2$ mass range could be copiously produced in the core. For $m_{\rm s} \sim 100$ keV$/c^2$ (where "s" stands for *sterile* neutrino), the vacuum mixing angle of sterile neutrinos is stringently constrained $\sin^2(2\theta) \lesssim 10^{-9}$ in order to avoid excessive energy loss [10] or to generate supernova asymmetries resulting in large pulsar kicks [20] (on alternative explanations for neutron star kicks, see, e.g., [21]). In the range 10 MeV$/c^2 \lesssim m_{\rm h} \lesssim m_K$ (where "h" stands for *heavy* sterile neutrino, and m_K is the Kaon mass), the constraints predominantly come from reactor anomalies and decays of pions and kaons. Furthermore, sterile neutrinos have been considered as a warm dark matter candidate [10,22–25], or as the origin of the 3.5 keV line observed in X-ray telescopes [26–28]. Here, we investigate the possible effects on the dynamics of supernova explosions and of the remnant PNSs of two such heavy sterile models: FKP of Fuller *et al.* [29] and AMP of Albertus *et al.* [30]. The models include a sterile neutrino $\nu_{\rm h}$ that has a relatively large mass ($m_{\rm h} \approx 200$ MeV$/c^2$ in FKP and $m_{\rm h} \approx 50$ MeV$/c^2$ in AMP) and is unstable ($\tau_{\rm h} \approx 100$ ms in FKP and $\tau_{\rm h} \approx 1$ ms in AMP). In both cases, the $\nu_{\rm h}$ is much heavier and shorter lived than the sterile neutrinos usually considered in oscillation analyses [31]. Notice that, once they are produced in a PNS, a lifetime longer than $\tau_{\rm h} > 1$ s would imply that the sterile neutrinos escape the central regions of the star but decay too far outside to have an impact on the dynamics of the regions where the stalled shock wave is revived, whereas for $\tau_{\rm h} < 10^{-7}$ s, they are unable to scape and are just reabsorbed by the core. The latter possibility may, however, have some impact on the core dynamics, since sterile neutrinos may add another channel to homogenize the core entropy and, therefore, damp convective instabilities. The lifetimes proposed in the two models evade cosmological bounds (the heavy neutrinos decay before primordial nucleosynthesis) and do not significantly affect stars like the Sun (they are too heavy to be produced there). However, as discussed in [29,30], these neutrinos may play a role in the transfer of energy to the stalled shock front during a supernova explosion. Using the numerical code Aenus [32,33], we will study quantitatively if this is the case and will estimate the optimal value of the parameters in the models in order to facilitate the SN explosion.

The manuscript is structured as follows. In Sec. II, we describe the models that we consider in this work. In Sec. III, we explain how to incorporate the production and the transport of the heavy sterile neutrinos in our one-dimensional core-collapse supernova (CCSN) simulations. In Sec. IV, we present our results, studying their dependence on the parameters of the models, and we conclude in Sec. V. In the Appendix, we provide tables detailing the production rate of sterile neutrinos as a function of temperature, electron chemical potential and sterile mass for the AMP model as well as discuss approximations that we made when calculating opacities of sterile neutrinos.

II. HEAVY STERILE NEUTRINO MODELS

Consider an $\mathrm{SU}(2)_L$-singlet Dirac neutrino $\nu_{\rm h}$ much heavier than the active ones. We may denote by N and N^c the two-component spinors that define $\nu_{\rm h}$:

$$\nu_{\rm h} = \begin{pmatrix} N \\ \bar{N}^c \end{pmatrix}. \tag{1}$$

After the breaking of the electroweak symmetry, this sterile neutrino may mix with an active one, ν, that may correspond to a single flavor or to a combination of flavors. The result is a mass eigenstate, $\nu'_{\rm h} = (N' \bar{N}^c)$ with

$$N' = \cos\theta N + \sin\theta \nu, \tag{2}$$

that inherits the gauge couplings of ν but suppressed by a factor of $\sin\theta$. Integrating out the W and Z bosons, we obtain the dimension-six operators

$$-\mathcal{L}_{\rm eff} \supset \frac{G_{\rm F} \sin\theta}{\sqrt{2}} [\bar{f}\gamma_\mu (C_V - C_A\gamma_5) f \bar{\nu}_{\rm h}\gamma^\mu(1-\gamma_5)\nu + \bar{f}'\gamma_\mu(1-\gamma_5) f \bar{\nu}_{\rm h}\gamma^\mu(1-\gamma_5)\ell] + \text{H.c.}, \tag{3}$$

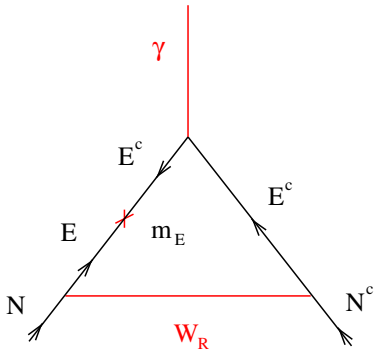

FIG. 1. One-loop diagram generating a magnetic dipole moment $\mu_{\rm h}$ for $\nu_{\rm h} = (N\tilde{N}^c)$. Changing $N \to \tilde{N}$, $E \to \tilde{E}$ and $m_E \to m_{\tilde{E}E}$ we obtain an electromagnetic dipole transition $\mu_{\rm tr}$ between ν (the active neutrino mixed with $\tilde{N}$) and $\nu_{\rm h}$.

where $G_{\rm F} = 1.16 \times 10^{-5}$ GeV$^{-2}(\hbar c)^3$ is the Fermi constant, γ_μ are the standard Dirac matrices, $\gamma_5 = i\gamma_0\gamma_1\gamma_2\gamma_3$, C_V and C_A are the vector and axial coupling constants, respectively, and we have dropped the prime to indicate mass eigenstates. Furthermore, ℓ is the charged lepton belonging to the same family as ν, and (ff') are standard fermions in the same SU$(2)_L$ doublet. These couplings imply the decays $\nu_{\rm h} \to \nu\bar{\nu}\nu$ and, if kinematically possible, $\nu_{\rm h} \to \nu\pi^0$, $\ell^-\pi^+$, $\ell^-\ell^+\nu$, whereas the dominant production channel in a PNS could be $\bar{\nu}\nu \to \bar{\nu}\nu_{\rm h}$ [29].

The sterile neutrino $\nu_{\rm h}$, however, may also obtain a different type of couplings: dimension-five operators generated not by mixing but through one-loop diagrams involving massive charged particles [6]. Let us be more specific. Suppose that at the TeV scale, we have a left-right (L − R) symmetric extension of the SM, and that the spinors N and N^c come in SU$(2)_R$ doublets together with a charged lepton:

$$L = \begin{pmatrix} N \\ E \end{pmatrix}, \qquad L^c = \begin{pmatrix} N^c \\ E^c \end{pmatrix}. \tag{4}$$

The breaking of the L − R symmetry may then result into a very massive charged lepton, $m_E \approx 1$ TeV$/c^2$, and a much lighter sterile neutrino, $m_{\rm h} = 0.01$–1 GeV$/c^2$. In this case, diagrams like the one in Fig. 1 will generate a magnetic dipole moment $\mu_{\rm h}$ for $\nu_{\rm h}$ that is suppressed by only one power of the L − R scale [34]:

$$-\mathcal{L}_{\rm eff} \supset \mu_{\rm h}\bar{\nu}_{\rm h}\sigma_{\mu\nu}\nu_{\rm h}\partial^\mu A^\nu, \tag{5}$$

where $\sigma_{\mu\nu} = i[\gamma_\mu, \gamma_\nu]/2$. Moreover, the possible mixing of a *different* sterile $\tilde{\nu}_{\rm h}$ (that could have a TeV$/c^2$ mass) with the active neutrino ν may generate an electromagnetic dipole transition $\mu_{\rm tr}$ between $\nu_{\rm h}$ and ν of the same order even if the $\nu\nu_{\rm h}$ mixing is negligible:

$$-\mathcal{L}_{\rm eff} \supset \frac{1}{2}\mu_{\rm tr}\bar{\nu}_{\rm h}\sigma_{\mu\nu}(1-\gamma_5)\nu\partial^\mu A^\nu + \text{H.c.} \tag{6}$$

These couplings will introduce photon-mediated interactions of the sterile neutrino $\nu_{\rm h}$ with the standard quarks and leptons. In particular, the dominant production channel in a PNS is expected to be $e^+e^- \to \bar{\nu}_{\rm h}\nu_{\rm h}$, whereas $\nu_{\rm h}$ will decay $\nu_{\rm h} \to \nu\gamma$ [35].

As mentioned, for a 1–500 MeV$/c^2$ heavy neutrino, the dominant bounds on any model come from cosmology and from data on the (semi)leptonic decays of mesons (pions, kaons, heavy mesons) and charged leptons. In all the cases of interest its lifetime must be $\tau_{\rm h} < 0.2$ s [36], so that in the early universe sterile neutrinos decay before primordial nucleosynthesis. If the lifetime is longer than 10^{-7} s the heavy neutrino becomes quasistable in laboratory experiments; i.e., it tends to decay after crossing any detector. $\nu_{\rm h}$ may then appear instead of the active ν in a fraction $\mathcal{O}(\sin^2\theta \approx |U_{i\rm h}|^2)$ of meson and muon decays. Notice that the larger the mass the more $\nu_{\rm h}$ may upset the kinematics in the process.

Masses $m_{\rm h} \leq 30$ MeV$/c^2$ are constrained only when $\nu_{\rm h}$ is mixed with the electron flavor: $\pi^+ \to e^+\nu$ puts bounds $|U_{e\rm h}|^2 \leq 10^{-6}$ at TRIUMF [37], with even stronger bounds for masses up to 130 MeV$/c^2$. At $m_{\rm h} = 30$–80 MeV$/c^2$ muon decays constrain the mixing with the ν_μ: $|U_{\mu\rm h}|^2 \leq 10^{-3}$ (see discussion in [35]). This mixing is very constrained by recent analyses [38,39]: $|U_{\mu\rm h}|^2 \leq 10^{-8}$ at $m_{\rm h} =$ 200–300 MeV$/c^2$ [38] and $|U_{\mu\rm h}|^2 \leq 2 \times 10^{-7}$ at $m_{\rm h} =$ 300–400 MeV$/c^2$ [39]. Combined with bounds from cosmology, these limits basically exclude the muon possibility in the FKP model. The bounds on the mixing with the tau flavor, from D_s meson and τ decays, are much weaker: around $|U_{\tau\rm h}|^2 \leq 10^{-4}$ for $m_{\rm h} > 160$ MeV$/c^2$ [40].

As for the dimension-six operators, for a 10^{-7}–0.1 s lifetime the heavy neutrino becomes invisible at colliders (no bounds on $\mu_{\rm h}$ and $\mu_{\rm tr}$) when the mixings vanish. In this limit, any purely electromagnetic process giving these neutrinos will be shadowed by an analogous Z-mediated process involving light neutrinos. In addition, the dominant decay mode $\nu_{\rm h} \to \nu\gamma$ may relax the bounds on the mixings [35] and provide an explanation for the MiniBooNE anomaly [41].

A. FKP model

The heavy neutrino proposed in [29] interacts with matter through $W^\pm$, Z boson exchange, with couplings generated through mixing ($\sin^2\theta < 10^{-4}$) with the ν_τ flavors. We set $m_{\rm h} = 200$ MeV$/c^2$ as the reference value for the mass. The main decay channel is $\nu_{\rm h} \to \nu_\tau\pi^0 \to \nu_\tau\gamma\gamma$, with a lifetime

$$\tau_{\rm h} \approx 66 \text{ ms}\left(\frac{5\times10^{-8}}{\sin^2\theta}\right)\left(\frac{200 \text{ MeV}}{m_{\rm h}c^2}\right)^3\left(\frac{0.54}{1-m_\pi^2/m_{\rm h}^2}\right), \tag{7}$$

where $m_\pi = 135\ \mathrm{MeV}/c^2$. In the hot PNS this ν_h will be produced predominantly through neutrino pair annihilation

$$\begin{aligned}\bar{\nu}_\tau\nu_\tau &\to \bar{\nu}_\tau\nu_\mathrm{h},\\ \bar{\nu}_\mu\nu_\mu &\to \bar{\nu}_\tau\nu_\mathrm{h},\\ \nu_\mu\nu_\tau &\to \nu_\mu\nu_\mathrm{h},\\ \nu_\tau\nu_\tau &\to \bar{\nu}_\mu\nu_\mathrm{h}.\end{aligned} \tag{8}$$

Other processes like pair production through nucleon-nucleon bremsstrahlung [42] will give subleading contributions due to large mass of the heavy neutrinos. A fit of the differential luminosity in sterile neutrinos gives

$$Q_\mathrm{FKP} \approx 3\times 10^{34}\frac{\mathrm{erg}}{\mathrm{cm^3 s}}\left(\frac{\sin^2\theta}{5\times 10^{-8}}\right)^2\left(\frac{k_\mathrm{B}T}{35\ \mathrm{MeV}}\right)^{7.2}e^{-\Theta_\mathrm{h}}, \tag{9}$$

where $\Theta_\mathrm{h} \equiv \frac{m_\mathrm{h}c^2}{k_\mathrm{B}T}$. We define

$$q_\mathrm{FKP} \equiv \left(\frac{\sin^2\theta}{5\times 10^{-8}}\right)^2 \tag{10}$$

and rewrite Eq. (9) as

$$Q_\mathrm{FKP} \approx 3\times 10^{34}\frac{\mathrm{erg}}{\mathrm{cm^3 s}}q_\mathrm{FKP}\left(\frac{k_\mathrm{B}T}{35\ \mathrm{MeV}}\right)^{7.2}e^{-\Theta_\mathrm{h}}. \tag{11}$$

The parameter q_FKP can be interpreted as a production rate efficiency with respect to the default value $\sin^2\theta = 5\times 10^{-8}$.

The heavy neutrinos will appear with a typical Lorentz factor of $\gamma_\mathrm{h} \lesssim 1.5$ [see Eq. (B3)], and their couplings to matter are so small that, once produced, they escape the core unscattered. Therefore, the only effect to consider as a ν_h propagates is its possible decay $\nu_\mathrm{h} \to \nu_\tau\gamma\gamma$ on a timescale given by Eq. (7). The initial energy carried by the heavy neutrino will be shared by the active ν_τ and the two photons (that result from the decay of the neutral pion) which will take a fraction

$$x_{\gamma\gamma} \approx 0.5(1 + m_\pi^2/m_\mathrm{h}^2) \tag{12}$$

of energy.

We finally note that the FKP model was proposed only in the $m_\mathrm{h} = 145 - 250\ \mathrm{MeV}/c^2$ mass range, and its extrapolation to higher masses is not straightforward. For example, at $m_\mathrm{h} \gtrsim 300\ \mathrm{MeV}/c^2$ (the heaviest neutrinos considered in our simulations), there will be new decay channels, like

$$\nu_\mathrm{h} \to \nu_\tau\pi^+\pi^-, \tag{13}$$

that will reduce the lifetime of the sterile neutrino. Including such effects is beyond the scope of this paper, however.

B. AMP model

In the AMP model [30], the dominant interactions of ν_h with matter are electromagnetic. A magnetic dipole moment (the superindex indicates the reference value)

$$\mu_\mathrm{h}^\mathrm{ref} = 10^{-9}c^{3/2}\hbar^{3/2}\ \mathrm{MeV}^{-1} = 3.4\times 10^{-9}\mu_\mathrm{B}, \tag{14}$$

where $\mu_\mathrm{B} \equiv e\hbar/(2m_e c)$ is the Bohr magneton with e being the elementary charge, implies that the dominant production channel in PNSs is

$$e^+e^- \to \bar{\nu}_\mathrm{h}\nu_\mathrm{h}. \tag{15}$$

The main decay mode, $\nu_\mathrm{h} \to \nu_{\mu,\tau}\gamma$, defines a lifetime

$$\tau_\mathrm{h} \approx 2.6\ \mathrm{ms}\left(\frac{\mu_\mathrm{tr}^\mathrm{ref}}{\mu_\mathrm{tr}}\right)^2\left(\frac{50\ \mathrm{MeV}/c^2}{m_h}\right)^3 \tag{16}$$

for the assumed reference value

$$\mu_\mathrm{tr}^\mathrm{ref} = 3.4\times 10^{-11}\mu_\mathrm{B} \tag{17}$$

of the dipole transition.

The coupling μ_tr also allows active to sterile transitions mediated by a photon and catalyzed by the presence of charged particles in the medium: $\nu_{\mu,\tau}X \to \nu_\mathrm{h}X$ where $X = p,\ e$. However, this contribution can be neglected since $\mu_\mathrm{tr} < \mu_\mathrm{h}$ and in the PNS the number density of $\nu_{\mu,\tau}$ is much smaller than that of electrons. The production rate of sterile neutrinos is

$$Q_\mathrm{AMP} = \left(\frac{\mu_\mathrm{h}}{\mu_\mathrm{h}^\mathrm{ref}}\right)^2 Q_\mathrm{TAB}(m_\mathrm{h}, \mu_\mathrm{e}, T), \tag{18}$$

where $Q_\mathrm{TAB}(m_\mathrm{h}, \mu_\mathrm{e}, T)$ is given by Table II (Appendix A). Note that the tabulated values are more precise than the original fit deduced in Eq. (24) of [30]. We define

$$q_\mathrm{AMP} \equiv \left(\frac{\mu_\mathrm{h}}{\mu_\mathrm{h}^\mathrm{ref}}\right)^2 \tag{19}$$

and rewrite Eq. (18) as

$$Q_\mathrm{AMP} = q_\mathrm{AMP}Q_\mathrm{TAB}(m_\mathrm{h}, \mu_\mathrm{e}, T). \tag{20}$$

The parameter q_AMP can be interpreted as a production rate efficiency with respect to the default value $\mu_\mathrm{h} = \mu_\mathrm{h}^\mathrm{ref}$.

An important difference with respect to the FKP model is that AMP neutrinos will not leave the PNS unscattered. The reason is that their cross section with matter, although much smaller that the ones involving active neutrinos, are

non-negligible. In particular, the propagation of ν_h is affected by the following three processes:

(1) The elastic scattering with protons. The approximate cross section for this process is [30]

$$\sigma_s \approx 7.5 \times 10^{-42}\ \mathrm{cm}^2 \left(\frac{\mu_h}{\mu_h^{\mathrm{ref}}}\right)^2. \tag{21}$$

We can neglect the ν_h scattering off electrons as the effect is only important for very energetic electrons, and due to Fermi-blocking such reactions will be reduced.

(2) The capture through inelastic collisions with charged particles: $\nu_h X \to \nu_{\mu,\tau} X$, with $X = p$, e. The cross section is given by

$$\sigma_a^X = a_X 10^{-45}\ \mathrm{cm}^2 \left(\frac{\mu_{\mathrm{tr}}}{\mu_{\mathrm{tr}}^{\mathrm{ref}}}\right)^2, \tag{22}$$

with $a_p = 0.9$ and $a_e = 2.1$ for proton and electron, respectively.

(3) The decay [with the lifetime given by Eq. (16)] into an active neutrino plus a photon, $\nu_h \to \nu_{\mu,\tau}\gamma$ that will take a fraction

$$x_\gamma \approx 0.5 \tag{23}$$

of the energy.

III. THE CODE

A. Hydrodynamics and active neutrinos

We added modules for evolving sterile neutrinos to a code developed for solving the coupled system of special relativistic (magneto)hydrodynamics (MHD) and active-neutrino transport [33] that was used before in multidimensional supernova modeling, e.g., [15, 43].

The methods for solving hyperbolic equations, i.e., high-order spatial reconstruction, and explicit Runge-Kutta (RK) time integration, are the basis for a very high accuracy of the solution of the MHD equations [44]. In the simulations presented in this paper, we use a monotonicity-preserving scheme of the fifth order (MP5; [45]), a third-order RK time integrator, and the HLL Riemann solver [46] The equations can be closed by any (tabulated) equation of state (EOS). Here, the EOS of [47] (LS-220) with an incompressibility modulus of 220 MeV is used. We add the fluid self-gravity using a quasirelativistic potential (case 'A' of [48]).

The active neutrinos are treated in the spectral, i.e., energy-dependent, hyperbolic two-moment formulation of the transport equation, which allows for the use of the same methods as for the MHD equations. This scheme is based on the expansion of the radiative intensity in its zeroth and first angular moments, i.e., the energy and momentum densities of the neutrinos, E and $\boldsymbol{F}$, respectively, and closing the system of equations by a local algebraic relation for the second moment, the radiation pressure tensor, P^{ij}. Among several possible choices for P^{ij}, we select the one based on the maximum-entropy Eddington factor. Consequently, we solve for each active neutrino species (in our case, three: ν_e, $\bar{\nu}_e$, and ν_X comprising all the other flavors) and for each neutrino energy, ε, a system of one scalar and one vector equation:

$$\begin{aligned}&\partial_t E + \partial_t v_i F^i + \nabla_i \alpha (F^i + v^i E)\\ &\quad - (\nabla_i \alpha + \dot{v}_i)[\partial_\epsilon(\epsilon F^i) - F^i]\\ &\quad - \nabla_i(\alpha v_j)[\partial_\epsilon(\epsilon P^{ij}) - P^{ij}] = \alpha Q_0,\end{aligned} \tag{24}$$

$$\begin{aligned}&\partial_t(F^i + v_j P^{ij}) + \nabla_j(\alpha P^{ij} + v^j F^i) + \dot{v}^i E\\ &\quad + \alpha F^j \nabla_j v^i + (E + P^j_j)\nabla^i \alpha\\ &\quad - \partial_\epsilon(\epsilon P_{ij})\dot{v}^j - \alpha \partial_\epsilon(\epsilon U^{ki}_j)\nabla_k v^j\\ &\quad - \partial_\epsilon(\epsilon P^{ij})\nabla_j \alpha = \alpha Q^i,\end{aligned} \tag{25}$$

where i and j are indices which run across the three spatial dimensions. The equation for the moment of degree n contains the divergence of a flux involving the moment of degree $n+1$ and a term describing the advection with the local fluid velocity, $\boldsymbol{v}$. This term of the equations is hyperbolic and is treated by the same methods as the MHD equations. Velocity and gravity are included in the $\mathcal{O}(v/c)-$plus approximation of [49]. Velocity terms represent Doppler shifts and aberration and the effects of fluid acceleration, while gravitational redshift and aberration are contained in the terms involving the lapse function, α, which we approximate as a function of the gravitational potential as $\alpha = \exp(\phi/c^2)$.

The source terms, Q, on the rhs of the moments equations describe the exchange of energy, momentum, and lepton number in reactions between neutrinos and matter. Therefore, they have exact counterparts in the energy, momentum, and electron fraction equations of the MHD system. We use a comprehensive set of reactions containing the absorption and emission of neutrinos by charged-current reactions of nucleons and nuclei and by pair processes (annihilation of electron-positron pairs and nucleon-nucleon bremsstrahlung) and scattering off nucleons, nuclei, and electrons/positrons (in the latter case, also accounting for energy transfer in nonisoenergetic scattering). Because the possibly very short time scales of reactions between matter and neutrinos can make terms very stiff, we employ implicit time integrators for their solutions.

Tests performed by [33] demonstrate that the code produces results that agree very well with the known solutions of simple problems and, in the case of core collapse simulations, with those given by state-of-the-art Boltzmann codes.

B. Sterile neutrino transport

We adopted the same transport scheme for the sterile neutrinos. However, lacking expressions for the dependence of their reactions with matter on their energy, we simplified the problem by using the set of grey, rather than spectral, moments equations, integrating Eqs. (24) and (25) over ε. We note that the two-moment system is, strictly speaking, valid only for massless particles (propagating at the speed of light) and using it for massive sterile neutrinos is not fully accurate and justified. However, both kinds of simplifications should not exceed the uncertainties related to input physics from the sterile neutrino models. This is why, we find using this scheme justified for the kind of exploratory study that reported here.

The most important ingredients that we take from the theory of sterile neutrinos are the rates at which sterile neutrinos are produced, their decay, and cross sections for their scattering off matter. In the two-moment scheme, the latter two processes contribute to the total opacity

$$\kappa = \kappa_{\rm a} + \kappa_{\rm s}, \tag{26}$$

where "a" and "s" stand for absorption and scattering, respectively. The opacity has units of cm^{-1}, i.e., $\kappa = \sigma n$, where σ is a cross section and n is the number density of target particles such as nucleons, nuclei, or electrons. In Eq. (24), only processes that exchange energy between neutrinos and matter appear. The source term reads

$$Q_0 = Q_{\rm p} - c\kappa_{\rm a} E, \tag{27}$$

where $Q_{\rm P} = Q_{\rm FKP/AMP}$ is the production term in the FKP or AMP model given by Eq. (9) or Table II in Appendix A, respectively. Scattering and absorption reactions contribute to the momentum exchange, leading to the source term

$$Q^i = -(\kappa_{\rm a} + \kappa_{\rm s}) F^i. \tag{28}$$

Within this framework, we can incorporate the reaction rates of AMP and FKP using the same numerical algorithm despite the physical differences between both models.

In the following calculations, we assume that $\gamma_{\rm h}\beta_{\rm h} \approx 1$, where $\beta_{\rm h} \equiv v_{\rm h}/c$ is the sterile neutrino velocity in terms of the speed of light. A more detailed discussion on the validity of this approximation can be found in Appendix B.

In the AMP model, the absorption opacity can be estimated with the help of Eqs. (16) and (22) as

$$\kappa_{\rm a} = \left[(0.9n_p + 2.1n_e)10^{-45} + 1.2\times 10^{-11}\left(\frac{m_{\rm h}c^2}{50\ \mathrm{MeV}}\right)^3\right] \times \left(\frac{\mu_{\rm tr}}{\mu_{\rm tr}^{\rm ref}}\right)^2 \mathrm{cm}^{-1}, \tag{29}$$

where $n_{\rm e}$ and n_p are the number densities $[\mathrm{cm}^{-3}]$ of electrons and protons, respectively. Furthermore, using Eq. (21), we obtain

$$\kappa_{\rm s} = 7.5\times 10^{-42} n_p \left(\frac{\mu_{\rm h}}{\mu_{\rm h}^{\rm ref}}\right)^2 \mathrm{cm}^{-1}. \tag{30}$$

In FKP model, the total opacity is given by

$$\kappa = \kappa_{\rm a}, \tag{31}$$

(i.e., there is no scattering opacity) and using Eq. (7), we estimate

$$\kappa_{\rm a} = 9.4\times 10^{-10}\left[\left(\frac{m_{\rm h}c^2}{200\ \mathrm{MeV}}\right)^3 - 0.46\left(\frac{m_{\rm h}c^2}{200\ \mathrm{MeV}}\right)\right]\mathrm{cm}^{-1}. \tag{32}$$

We also assume that once sterile neutrinos decay, the energy (and momentum) carried by created photons (given by Eqs. (23) and (12) in the AMP and FKP models, respectively) will be reabsorbed by matter and converted into thermal energy. The energy (and momentum) carried by the active neutrino created in the decay will be, depending on the density where the decay occurs, carried away from the system if $\rho < 10^{10}\ \mathrm{g\,cm}^{-3}$ or reabsorbed by the system because of the neutrino trapping for $\rho > 10^{12}\ \mathrm{g\,cm}^{-3}$. For densities $10^{10}\ \mathrm{g\,cm}^{-3} < \rho < 10^{12}\ \mathrm{g\,cm}^{-3}$, we use a logarithmic interpolation between these two regions. Note that this is a phenomenological prescription that we use instead of generating another active neutrino in the code. To test the influence of this assumption on the simulation results, we performed two additional models A4a and A4b, which have all parameters like model A4, but threshold densities for the transition region $10^{11}\ \mathrm{g\,cm}^{-3} < \rho < 10^{13}\ \mathrm{g\,cm}^{-3}$, and $10^{12}\ \mathrm{g\,cm}^{-3} < \rho < 10^{14}\ \mathrm{g\,cm}^{-3}$, respectively (see Sec. IV and Table I).

Taking into account the large uncertainties in all processes involved and the relatively simple approach for modeling the sterile neutrinos (nonspectral transport, no velocity terms, assumptions on the neutrino velocity and Lorentz factor), we will consider neutrinos with a lifetime of up to $\tau_{\rm h} = 1$ s, i.e., exceeding the bound from primordial nucleosynthesis, but still of the same order of magnitude.

C. Numerical setup

For this study, we restrict ourselves to spherical symmetry and single progenitor star of zero age main sequence mass $M_{\rm ZAMS} = 15\ M_\odot$, namely model s15s7w2 of [50]. We deem the latter restriction justified as our goal is not arriving at detailed predictions for specific stars. Therefore, we selected a standard star whose evolution is well understood as it served as a test case in several previous studies. The spherical symmetry certainly limits the applicability of

TABLE I. Simulations performed with active neutrinos (R–*reference model*) or additionally sterile neutrinos of the AMP model (A) or the FKP model (F). The columns from left to right give: sterile neutrino model, sterile neutrino mass, production efficiency with respect to the default parametres in the AMP [Eq. (19)] and the FKP [Eq. (10)] models, transition moment [Eq. (17)], and sterile neutrino mean free path (neglecting scattering). In the case of a successful explosion, further columns give: explosion time, explosion radius, remnant mass and explosion energy. These latter three quantities are determined at the end of the simulation (given in the last column) and can change with time.

#	$m_h c^2$ [MeV]	q	μ_{tr} $[\mu_{tr}^{ref}]$	$\tau_h c$ [km]	t_{expl} [ms]	r_{expl} [km]	M_c $[M_\odot]$	E_{expl} [erg]	t_{end} [ms]
R	…	…	…	…	…	…	…	…	1000
A1	50	1	10	7.9	…	…	…	…	1000
A2	50	1	6	22	248	29	1.40	2.7×10^{51}	468
A3	50	1	3	88	78	32	1.22	1.1×10^{52}	283
A4	50	1	1	790	36	40	1.26	4.2×10^{52}	168
A4a	50	1	1	790	36	40	1.26	4.3×10^{52}	164
A4b	50	1	1	790	36	40	1.27	4.3×10^{52}	159
A4D	50	1	1	790	36	44	1.26	3.4×10^{52}	135
A4T	50	1	1	790	37	42	1.26	3.6×10^{52}	136
A5	50	1	0.5	3200	38	46	1.30	4.6×10^{52}	149
A6	50	1	0.3	8800	41	53	1.33	3.7×10^{52}	148
A7	50	1	0.1	7.9×10^4	65	1700	1.49	1.8×10^{52}	288
A8	50	1	0.05	3.2×10^5	90	4100	1.65	1.3×10^{52}	652
A9	50	0.3	6	22	246	53	1.42	8.9×10^{50}	332
A10	50	0.3	3	88	85	29	1.25	1.3×10^{52}	324
A11	50	0.3	1	790	50	41	1.29	4.6×10^{52}	220
A12	50	0.3	0.3	8800	59	44	1.36	4.2×10^{52}	208
A13	50	0.3	0.1	7.9×10^4	89	1600	1.49	1.5×10^{52}	293
A14	50	0.1	6	22	253	39	1.42	2.1×10^{51}	439
A15	50	0.1	3	88	103	27	1.29	1.5×10^{52}	372
A16	50	0.1	1	790	68	43	1.32	4.5×10^{52}	229
A17	50	0.1	0.3	8800	81	55	1.39	4.6×10^{52}	250
A18	50	0.1	0.1	7.9×10^4	117	1300	1.49	1.4×10^{52}	335
A19	50	3×10^{-2}	3	88	136	26	1.35	1.5×10^{52}	425
A20	50	3×10^{-2}	1	790	98	37	1.36	4.8×10^{52}	322
A21	50	3×10^{-2}	0.3	8800	112	55	1.43	3.9×10^{52}	292
A22	50	3×10^{-2}	0.1	7.9×10^4	153	5300	4.60	1.0×10^{45}	152
A23	50	10^{-2}	1	790	132	41	1.26	1.9×10^{52}	228
A24	50	10^{-2}	0.3	8800	148	61	1.46	3.1×10^{52}	336
A25	50	10^{-2}	0.1	7.9×10^4	193	2900	1.61	1.6×10^{51}	265
A26	50	3×10^{-3}	0.3	8800	197	26	1.48	1.4×10^{52}	385
A27	50	3×10^{-3}	0.1	7.9×10^4	249	3400	1.65	4.2×10^{51}	494
A28	50	10^{-3}	0.1	7.9×10^4	310	4500	1.73	4.4×10^{51}	807
A29	50	0.2	2	200	67	34	1.27	1.9×10^{52}	284
A30	80	1	1	190	73	41	1.26	1.9×10^{52}	227
F1	150	0.2	…	6.7×10^5	870	2.6×10^4	2.55	6.6×10^{49}	1000
F2	150	1	…	1.3×10^5	464	6300	1.85	3.0×10^{51}	1000
F3	150	2	…	6.7×10^4	382	2000	1.64	6.6×10^{51}	878
F4	150	6	…	2.2×10^4	285	21	1.53	9.1×10^{51}	478
F5	150	20	…	6700	218	53	1.48	4.7×10^{52}	397
F6	150	60	…	2200	166	52	1.45	6.6×10^{52}	316
F7	200	0.2	…	9.8×10^4	886	2.5×10^4	2.53	4.0×10^{49}	970
F8	200	1	…	2.0×10^4	582	4600	1.75	1.3×10^{51}	1000
F9	200	2	…	9800	493	210	1.59	1.9×10^{51}	715
F10	200	6	…	3300	369	65	1.52	2.1×10^{51}	437
F11	200	20	…	980	255	41	1.48	1.7×10^{52}	441
F12	200	60	…	330	210	33	1.46	3.2×10^{52}	453
F13	250	1	…	7700	…	…	…	…	1000

(Table continued)

TABLE I. *(Continued)*

#	$m_{\rm h}c^2$ [MeV]	q	$\mu_{\rm tr}$ $[\mu_{\rm tr}^{\rm ref}]$	$\tau_{\rm h}c$ [km]	$t_{\rm expl}$ [ms]	$r_{\rm expl}$ [km]	$M_{\rm c}$ $[M_\odot]$	$E_{\rm expl}$ [erg]	$t_{\rm end}$ [ms]
F14	250	2	…	3800	761	860	1.62	2.6×10^{50}	820
F15	250	6	…	1300	475	22	1.54	2.7×10^{50}	499
F16	250	20	…	390	349	38	1.51	3.1×10^{51}	452
F17	250	60	…	130	295	31	1.49	9.2×10^{51}	502
F18	250	200	…	39	349	38	1.51	3.1×10^{51}	452
F19	300	2	…	2000	…	…	…	…	957
F20	300	6	…	660	…	…	…	…	695
F21	300	20	…	200	527	21	1.56	3.6×10^{49}	535
F22	300	60	…	66	462	31	1.54	1.2×10^{51}	510
F23	300	200	…	20	…	…	…	…	691

the simulations to real stellar core collapse, but we accept it for such a first step towards exploring the principle order of magnitude of the effects of sterile neutrinos. If indeed our study indicate interesting effects, it should be followed up by a more thorough investigation with multidimensional simulations.

We set up the simulations by mapping the pre-collapse model to a grid of 608 zones extending to $r_{\rm max}=10^6$ km with spacing $\Delta r=0.0186r+0.2$ km. This numerical resolution has been chosen on the basis of our previous experience in the simulation of supernova explosions with standard active neutrinos, e.g., [15,51,52], as well as a convergence study whereby one of the models incorporating sterile neutrinos has been rerun with resolutions two and three times larger than in our default numerical set up (see Table I and the discussion in Sec. IV). We evolve the core with different settings for the sterile neutrinos through collapse up to 1s after bounce. Without sterile neutrinos, we observe the common outcome of core collapse in spherical symmetry, viz. the formation of a PNS and a failure of the SN explosion as the shock wave stalls at a maximum radius of 141 km and is never revived, eventually leading to collapse to a black hole (BH) on much longer times scales.

IV. RESULTS

We begin our analysis with the reference simulation (model R from Table I) which was run only with the three active neutrino flavors. For an overview of the evolution, we refer to the upper left panel of Fig. 2 displaying entropy, neutrino cooling and heating, and contours of the gas density as a function of time and radius, as well as shock, gain and electron-neutrinosphere radii. After bounce ($t=0$ ms), the shock wave of the reference model (green solid line) stalls at a maximum radius of $r_{\rm sh}=141$ km at $t\approx65$ ms. Afterwards, neutrino heating (mapped with shades of orange in the bottom subpanel) deposits energy in the postshock region as well as outside the shock. As a result, the entropy (the top subpanel) behind the shock increases and a standard *hot bubble* forms. The active neutrino heating, however, is insufficient to revive the shock wave. Hence, it slowly recedes to a radius of $r_{\rm sh}\approx30$ km at $t=1000$ ms. The contraction is briefly interrupted at $t\approx160$ ms when the density of the infalling matter quickly drops while its entropy increases as the surface of the iron core falls through the shock. The reduction of the ram pressure thereby produced is, nevertheless, insufficient to spur the escape of the receding shock, differently to what may happen in similar multidimensional rotating and magnetized models [15,53]. Taking the radius of the electron-neutrinospheres as a proxy for its radius (magenta line), we find that the PNS contracts gradually while it accretes matter. We note that the evolution continues for much longer than the 1000 ms of postbounce time shown here and ends once the accretion of matter increases the PNS mass beyond the stability limit imposed for self-gravitating objects, which for our EOS lies above a baryonic mass of $M_{\rm max}\gtrsim2.45\ M_\odot$. At that point, the PNS will collapse to a BH. The maximum temperature of the PNS (black solid line in Fig. 3, which is located at a radius marked with the dashed line of the same color) increases throughout the simulation, as more energy is provided to the PNS through accretion of mass and contraction (which releases gravitational energy; see the dashed lines in the figure) than extracted by the production of active neutrinos (neutrino cooling).

Next, we discuss the model A4 (from Table I, see the upper right panel of Fig. 2 as well as the left panel of Figs. 4, and 5) which was run with (apart from the active neutrinos) sterile neutrinos of AMP with the default parameters considered by those authors, i.e., $m_{\rm h}=50\ {\rm MeV}/c^2$, $\mu_{\rm h}=10^{-9}(\hbar c)^{3/2}\ {\rm MeV}^{-1}$ and $\mu_{\rm tr}=10^{-11}(\hbar c)^{3/2}\ {\rm MeV}^{-1}$.

The production of sterile neutrinos at the center of the core adds an additional channel for cooling. As model A4 demonstrates, the rate at which sterile neutrinos are produced (Fig. 4; blue dashed line), calculated as

$$\mathcal{Q}^{\rm h}_{\rm cool}\equiv\int Q_{\rm p}{\rm d}V, \tag{33}$$

can exceed the luminosity of active neutrinos significantly. At bounce, the cooling by sterile neutrinos

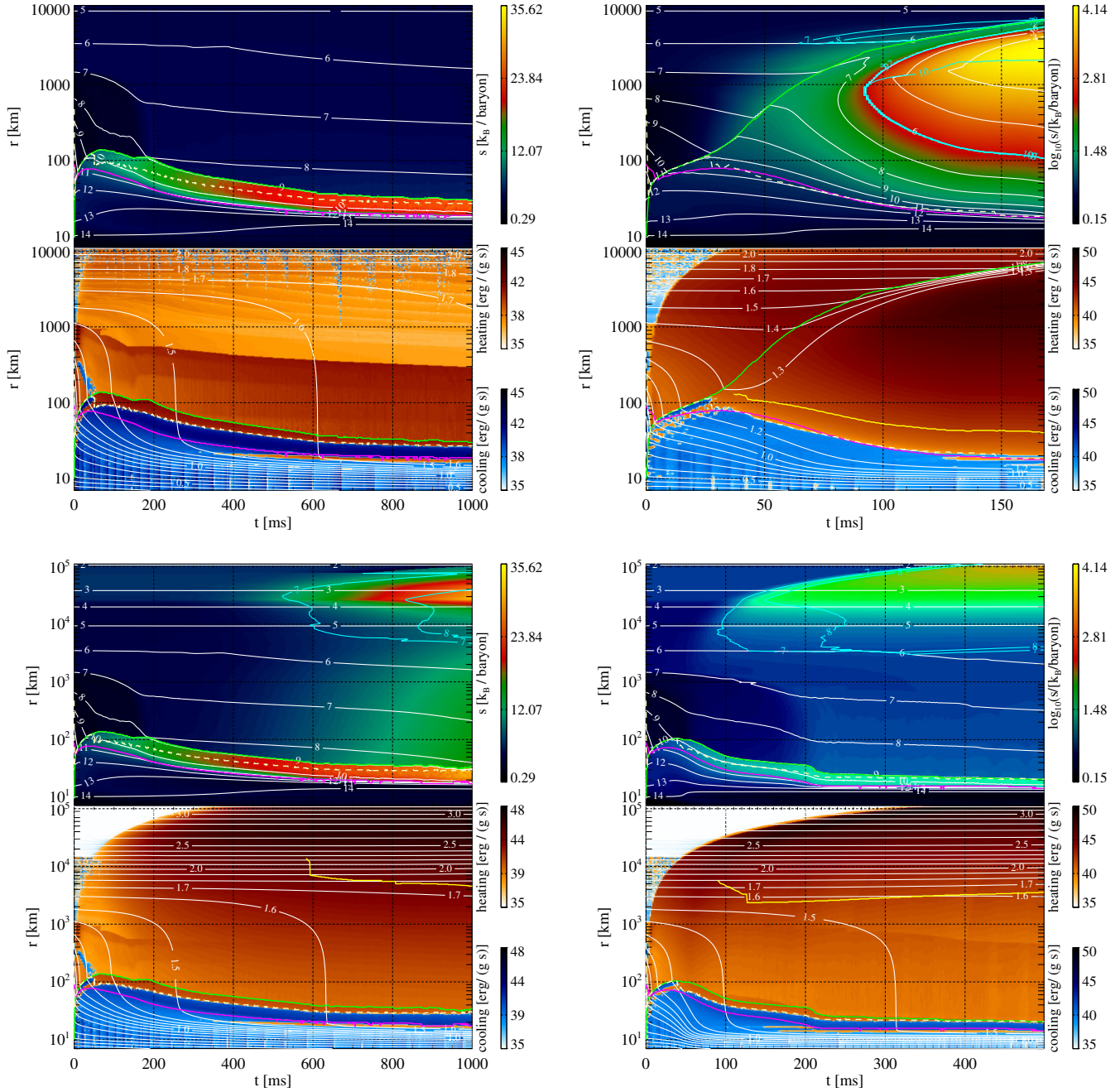

FIG. 2. Time evolution of models R (*top left*), A4 (*top right*), F8 (*bottom left*), and A8 (*bottom right*) from Table I. Upper subpanels: [logarithm of] entropy per baryon (color map), density ($\log_{10}(\rho/1\ \mathrm{g\,cm^{-3}})$; white isocontours), positive radial velocity ($\log_{10}(v_r/1\ \mathrm{cm\,s^{-1}})$; light blue isocontours). Lower subpanels: total (i.e., active and sterile) neutrino heating (shades of orange) and cooling (shades of blue), enclosed mass (in solar masses, white isocontour), explosion radius (yellow line). In both panels: shock radius (green line), neutrino sphere radius (proxy for the PNS radius; magenta), and gain radius (dashed salmon). Note that the color scales as well as the radial (vertical) and temporal (horizontal) scales may vary from panel to panel.

($\mathcal{Q}^{\mathrm{h}}_{\mathrm{cool}} \approx 10^{50}\ \mathrm{erg\,s^{-1}}$) is much lower than that by active neutrinos ($\gtrsim 10^{53}\ \mathrm{erg\,s^{-1}}$; with black solid line, neutrino luminosity L_ν is marked as its proxy). While the latter goes through the neutrino burst and then settles to a relatively constant value $L_\nu \sim 10^{53}\ \mathrm{erg\,s^{-1}}$, the production of sterile neutrinos is significantly enhanced due to a rapid increase of the central temperature (from $T = 12$ to $27\ \mathrm{MeV}/k_\mathrm{B}$; see the solid blue line in Fig. 3). Already at $t \approx 18$ ms both production rates become equal ($\approx 2 \times 10^{53}\ \mathrm{erg\,s^{-1}}$), and at $t \approx 67$ ms, the production rate of sterile neutrinos reaches its peak ($\mathcal{Q}^{\mathrm{h}}_{\mathrm{cool}} \approx 1.6 \times 10^{54}\ \mathrm{erg\,s^{-1}}$; $T \approx 27\ \mathrm{MeV}/k_\mathrm{B}$) being 1 order of magnitude larger than that of active neutrinos.

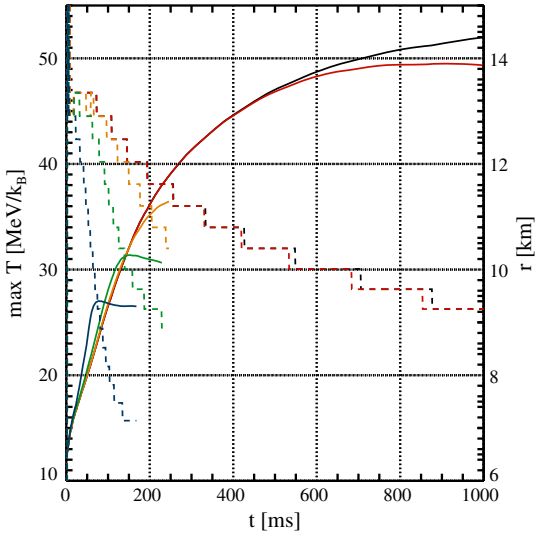

FIG. 3. Maximum temperature (solid lines) and its location (dashed lines) in models: R (black), F8 (red), A23 (orange), A16 (green), and A4 (blue).

Afterwards, the central temperature (and hence the production rate of sterile neutrinos) starts to slowly drop, reaching $T \approx 26\ \mathrm{MeV}/k_\mathrm{B}$ at $t = 168$ ms. As a consequence, the PNS loses energy at a higher rate and contracts faster. This can be clearly seen from the upper panels of Fig. 2, where the evolution of the (electron) neutrinosphere (as a proxy for the PNS radius) is marked with magenta for the reference (left) and A4 (right) models. At $t = 100$ ms, the PNS radius in the latter is $r \approx 26$ km, whereas in the former $r \approx 65$ km, (the radius $r \approx 26$ km being reached only at $t \approx 400$ ms).

The combination of a much more compact core together with a faster cooling contributed by the sterile neutrinos in model A4 yields much larger density gradients (of about 1 order of magnitude per grid zone) at the surface of the PNS in this model than in the reference one. These gradients grow with time and cause the code to fail after about 170 ms, because it cannot recover the thermal pressure in a narrow region exterior to the remnant PNS. However, this is not an insurmountable problem for the purpose of our study because the explosion takes place much earlier than the code failure,[2] allowing us to draw the qualitative conclusion that the action of sterile neutrinos makes viable the explosions of models which otherwise are not exploding.

Indeed, in order to guarantee that our results are minimally polluted by the finite grid resolution employed, we have rerun model A4 with double (model A4D) and triple (model A4T) number of grid zones. We find that the evolution of the explosion energy and of the unbound mass converge for the first $t \approx 130$ ms (Fig. 5) with small discrepancies appearing only shortly before the code failure. The explosion properties (t_expl, r_expl and E_expl) and the remnant mass (M_c) listed in Table I are compatible within $\lesssim$20% accuracy (the main reason of these slight deviations being different final simulation times).

Due to their short lifetime of 2.6 ms and because they suffer multiple elastic scatterings with charged matter, the sterile neutrinos in A4 model decay within the core and deposit a large fraction of their energy inside a radius $r = 790$ km. Thus, the temporal evolution of the total heating rate by sterile neutrinos

$$\mathcal{Q}^\mathrm{h}_\mathrm{heat} \equiv \int c\kappa_\mathrm{a} E \mathrm{d}V \tag{34}$$

(solid red line in the left panel of Fig. 4) is, except for a brief time delay, the same as that of their production (dashed blue line). Depending sensitively on gas density and temperature, the production term drops at the outer edge of the PNS. Consequently, all the gas outside the PNS is exposed to heating by the decaying sterile neutrinos at an extraordinarily large rate exceeding a lot that due to active neutrinos. Thus, the shock wave does not stall its expansion at all.

We compute the explosion energy and the ejecta mass (i.e., the unbound mass; see Fig. 5), respectively, as

$$E_\mathrm{expl} = \int_{r \geq r_\mathrm{expl}} e_\mathrm{tot} \rho \mathrm{d}V, \tag{35}$$

$$M_\mathrm{expl} = \int_{r \geq r_\mathrm{expl}} H(e_\mathrm{tot}) \rho \mathrm{d}V, \tag{36}$$

where H is the Heaviside step function and

$$e_\mathrm{tot} = e_\mathrm{kin} + e_\mathrm{grav} + e_\mathrm{int}, \tag{37}$$

with e_kin, e_grav, and e_int being the specific kinetic, binding (gravitational) and internal energy, respectively. The explosion radius, r_expl, (if exists) is defined as the innermost radius where the integral in Eq. (35), as well as both the radial velocity ($v_r(r_\mathrm{expl}) > 0$) and total specific energy of the fluid element, e_tot, are positive. We define the explosion time as the moment when such an explosion radius is found. The (time dependent) explosion radius r_expl is marked with a yellow line in the bottom half of the middle panel of Fig. 2. Note that according to our definition, not necessarily all fluid elements located at $r > r_\mathrm{expl}$, have positive e_tot (there can be layers of the star, sufficiently far above r_expl, where $e_\mathrm{tot} < 0$ since they have not been affected by the explosion dynamics yet). However, the total energy is sufficient to unbind even the gas with a negative total energy outside r_expl. Indeed, in model A4, $M_\mathrm{expl} = 0.64\ M_\odot$ (black dashed line in Fig. 5) by the end

[2]We note that in all models that could not be simulated until $t = 1000$ ms, we measure the explosion properties (given in Table I) typically $\gtrsim$10 ms before the code crash, so that they are not affected by numerical artifacts proceeding the code failure.

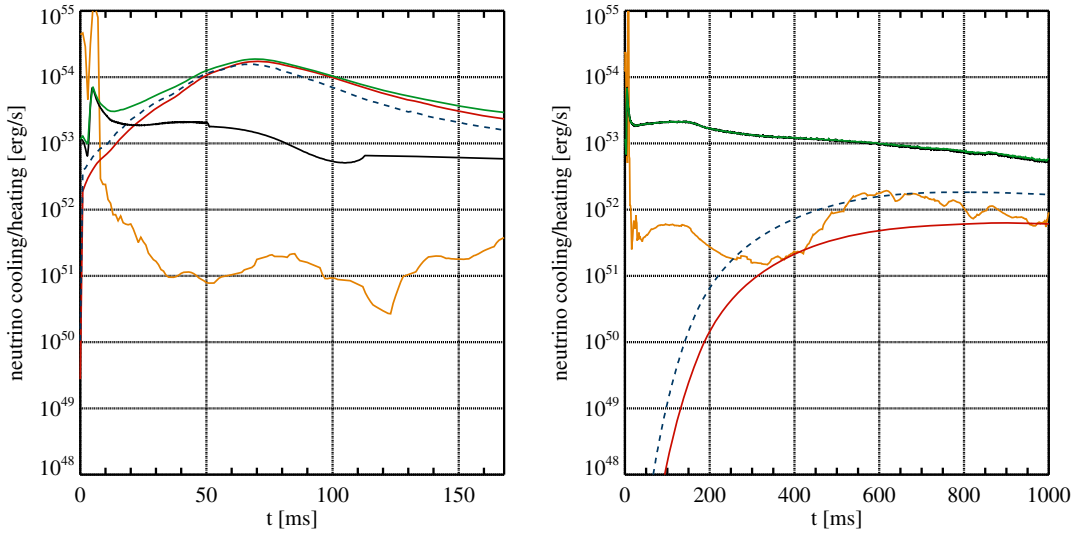

FIG. 4. Total (volume integrated) cooling rate due to active (black) and sterile (blue dashed line) neutrinos, and total heating rate due to active (orange) and sterile (red) neutrinos in A4 (*left*) and F8 (*right*) models from Table I. The cooling due to active neutrinos is equivalent to the luminosity they would have if only SM processes were included. The decays of sterile to active neutrinos add an additional contribution to their total luminosity, which is shown by the greed dash-dotted lines.

of simulation even though the mass contained between $r_{\rm expl}$ and $r_{\rm max}$ is 3.32 $M_\odot$. For model A4, we find an explosion as early as $t_{\rm expl} = 36$ ms; i.e., we might classify the model as a prompt explosion.

Once an explosion sets in and the gas surrounding the PNS reaches positive (radial) velocities, the accretion ceases (see the mass shell lines of 1.2 $M_\odot$ and 1.3 $M_\odot$ in Fig. 2). Hence, the growth of the PNS mass effectively stops at values of $M_{\rm PNS} \simeq 1.26\ M_\odot$ at $t = 168$. Thereby, this model is unlikely to produce a BH, even though the PNS may continue to contract as it loses internal energy by neutrino radiation.

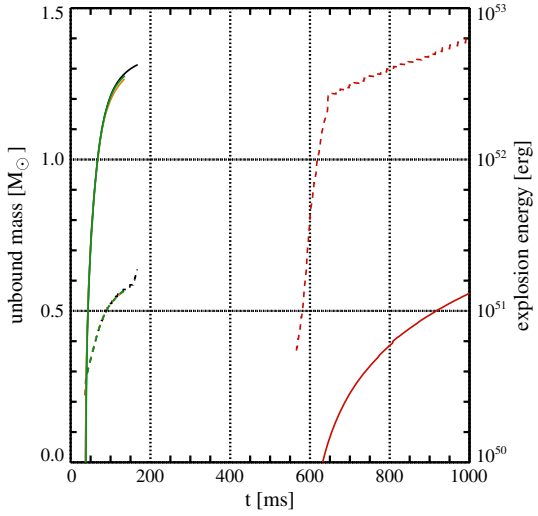

FIG. 5. Explosion energy (Eq. (35); solid lines) and unbound mass (Eq. (36); dashed lines) in A4 (black), A4D (orange), A4T (green), and F8 (red) models from Table I. Note the excellent agreement (convergence) between the models A4, A4D, and A4T for $t \lesssim 130$ ms.

The key difference between the heating by active and by sterile neutrinos is that the latter has a contribution that does not come from reactions between neutrinos and matter, but from the direct decays of sterile neutrinos. Therefore, the heating rate associated to this process does not depend on the local thermodynamics such as density, electron fraction, and temperature, but is directly given by the neutrino lifetime. Hence, sterile neutrinos can efficiently heat even cold matter at low densities where the interactions with active neutrinos are far too infrequent for active neutrinos to be significant. This effect leads to the asymptotic value of the absorption opacity for the sterile neutrinos at high radii (solid green line in Fig. 6), which exceeds that for active neutrinos (solid black line) outside of a few hundred km. It should be furthermore noted that the strong drop of the absorption opacities for the active neutrinos as well as the scattering opacities for both kinds of neutrinos at the location of the shock wave ($r_{\rm sh} \approx 70$ km) is not present in the absorption opacity of sterile neutrinos.

This important property of heating by sterile neutrinos causes several peculiar differences from explosions driven by active neutrinos. First of all, as neutrino heating is not essentially limited to the postshock layer, the explosion encompasses very quickly a very large radial range. The shock radius (green line in the right panel of Fig. 2) reaches a radius of $r_{\rm sh} \approx 7040$ km at $t = 168$ ms. At this point, $E_{\rm expl} = 4.2 \times 10^{52}$ erg and $M_{\rm expl} = 0.64\ M_\odot$, and the fastest outflow velocities exceed 2×10^{10} cm s^{-1}. All of these values are still rising by the end of the simulation (Fig. 5) Remarkably, the very high explosion energy is in the range of the most luminous hypernovae [54–56]. Secondly, as

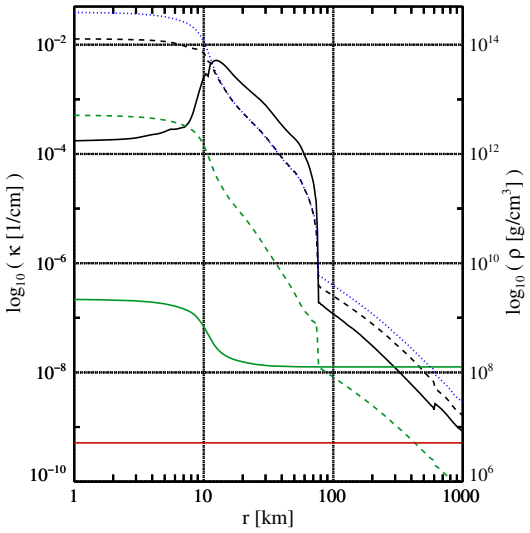

FIG. 6. Absorption (solid lines) and scattering (dashed lines) opacities of electron neutrinos with energies 75–101 MeV (i.e., the most populated energy bin; black) and of sterile neutrinos in simulation A4 (green) at $t = 10$ ms postbounce. With red solid line is marked the absorption opacity of sterile neutrinos in model F8. Density profile is marked with blue dotted line.

much of the heating occurs at relatively low densities and temperatures (note the high values of the *specific* heating rate; bottom subpanel of the upper right panel of Fig. 2 at $r > 1000$ km), the energy deposition corresponds to a very strong increase of the gas entropy. We find specific entropies in excess of $s > 10^4 k_B$/baryon in the ejecta and temperatures of $\gtrsim 0.5\ \mathrm{MeV}/k_B$. This combination of conditions should lead to events that strongly differ from the Standard Model for supernovae in terms of their observational properties as well as their nucleosynthethic yields. We note that a part of the energy of the decaying sterile neutrinos should go into active neutrinos, which will stream out from the place of their creation almost freely. Hence, also the light curves of active neutrinos should be strongly increased. We did not compute this effect, however.

As already mentioned in Sec. III B, we use a phenomenological prescription for the deposition of the energy and momentum of active neutrinos which are created as a result of sterile neutrino decays instead of generating them in the code and using the full transport equations. We chose by default that the energy and momentum of such neutrinos will be carried away from the system if they are created at $\rho < 10^{10}\ \mathrm{g\,cm^{-3}}$ (because their mean free path (MFP)—inverse of opacity—is $\gtrsim 10$ km; see Fig. 6) or reabsorbed by the system at $\rho > 10^{12}\ \mathrm{g\,cm^{-3}}$ (MFP $\lesssim 10$ m). In the transition region $10^{10}\ \mathrm{g\,cm^{-3}} < \rho < 10^{12}\ \mathrm{g\,cm^{-3}}$, a logarithmic interpolation between these two scenarios is used. To test the influence of the threshold densities, in models A4a and A4b, we set them to $10^{11}\ \mathrm{g\,cm^{-3}} < \rho < 10^{13}\ \mathrm{g\,cm^{-3}}$, and $10^{12}\ \mathrm{g\,cm^{-3}} < \rho < 10^{14}\ \mathrm{g\,cm^{-3}}$, respectively. As can be seen in Table I), their impact on the explosion properties is marginal.

Next, we discuss model F8 (Table I, see the bottom left panel of Fig. 2 as well as the right panel of Figs. 4 and 5) which was run with sterile neutrinos of FKP with the default parameters considered by those authors, i.e., $m_h = 200\ \mathrm{MeV}/c^2$ and $\sin^2\theta = 5 \times 10^{-8}$. The production rate [Eq. (9)] exhibits a considerably different dependence on the local thermodynamic conditions, most notably on temperature, with respect to the AMP model. Compared to model A4, it takes longer for sterile neutrinos to be generated at significant rates (cf. the dashed blue lines in the left and right panels of Fig. 4). Furthermore, their production rate saturates at a level that is about 1 order of magnitude below that of active neutrinos. Consequently, they only have a relatively minor influence on the evolution of the PNS whose thermal evolution and contraction are similar to those of the reference model. Within the time of the simulation (i.e., 1000 ms), the radii of the two PNSs differ only slightly, as shown by the top and bottom left panels of Fig. 2. The sterile neutrinos leave an imprint in the evolution of the maximum temperature of model F8 reaching a maximum of $T_{\max} \approx 49.5\ \mathrm{MeV}/k_B$ at $t \approx$ 900 ms, while it continuously rises to a final value of $T_{\max} \approx 52\ \mathrm{MeV}/k_B$ at the end of the simulation of model R (see the solid red and black lines, respectively, in Fig. 3).

Another difference between A4 and F8 models is that in the latter, sterile neutrinos have a much longer lifetime of $\tau_h = 66$ ms. This leads to two effects. First, there is a noticeable delay between the production of a sterile neutrino and its eventual decay. Hence, its energy is temporarily unavailable to the system. This causes a retardation of the heating by sterile neutrinos with respect to the cooling (see the right panel of Fig. 4). Second, and more importantly, sterile neutrinos typically travel a (much longer) distance of about $\tau_h c \approx 2 \times 10^4$ km before decaying. This is not only due to their much lower absorption opacity (see the red line in Fig. 6), but also because, unlike in the AMP model, once produced in the center, they propagate outwards unscattered. Hence, heating by sterile neutrinos does not occur behind the stalled shock, but rather outside the inner core. Consequently, model F8 also explodes, but does so in a very different way. The decaying neutrinos unbind matter at radii $r \gtrsim 4600$ km triggering an explosion at time $t_{\mathrm{expl}} \approx 582$ ms. The effect is most notable at several 10 000 km, where the deposition of a large amount of energy into gas of rather low density ($\rho \lesssim 10^4\ \mathrm{g\,cm^{-3}}$) lends itself to a strong increase of the entropy (the bottom left panel of Fig. 2). After heating for several hundreds of milliseconds, we find by the end of the simulation an explosion energy $E_{\mathrm{expl}} \approx 1.3 \times 10^{51}$ erg carried by a mass of $M_{\mathrm{expl}} \approx 1.4\ M_\odot$ with a maximum expansion velocity of $v_{\max} \approx 1.9 \times 10^8\ \mathrm{cm\,s^{-1}}$. Even though these values are within the range of standard CCSN explosions, we expect

this model to produce an electromagnetic signal significantly differing from common events because of the relative absence of heavy elements in the ejecta. This is because only matter from outside the iron core is unbound and the low densities and temperatures would suppress most reactions relevant to explosive nucleosynthesis. We point out that the aforementioned independence of the heating of local thermodynamic conditions is crucial for this explosion mechanism.

So far, we have only considered sterile neutrinos of AMP and FKP with the default parameters chosen by those authors. However, in both models, sterile neutrinos are characterized by, respectively, three and two free parameters that only have rough constraints from particle physics theory and experiments. In AMP, these are: mass, $m_{\rm h}$, magnetic dipole moment, $\mu_{\rm h}$, and dipole transition moment, $\mu_{\rm tr}$, whereas in FKP: mass, $m_{\rm h}$, and mixing angle, $\sin^2\theta$.

In simulations A1–A8, we vary the transition moment of the sterile neutrinos, $\mu_{\rm tr}$, which influences their lifetimes, $\tau_h = 2.6\times10^{-5},\ldots,1$ s, [Eq. (16)] and the cross section on their capture through inelastic collisions with charged particles [Eq. (22)]. For the shortest lifetimes (model A1), the sterile neutrinos travel only a few kilometeres from their production site before decaying. As a consequence, they do not contribute to the energy transmission from the PNS to outer layers. Instead, an equilibrium between matter and trapped neutrinos is established. The dynamics basically is the same as in the reference model; i.e., no explosion is launched.

Intermediate lifetimes, corresponding to typical propagation distances of several tens to hundreds of kilometeres result in successful shock revival.

The most long-lived neutrinos that we investigated (models A7 and A8; for the latter see the bottom right panel of Fig. 2) behave similarly to model F8 discussed above. Explosions are launched not by reviving the stalled shock wave, but by ejecting the outer shells of the star. However, sterile neutrinos are produced more efficiently than in model F8, which yields more energetic explosions. In fact, the explosion energies in models A7 and A8 are in the range of hypernovae. Furthermore, the matter unbound by neutrino heating reaches extremely high entropies in excess of $s \gtrsim 10^4\ k_{\rm B}$/baryon.

In simulations A4, A11, A16, A20, and A23, we vary the magnetic moment,$\mu_{\rm h}$, which influences the cross section of the sterile neutrinos for elastic scattering with protons [Eq. (21)], and, more importantly, their production rate [Eq. (18)]. Figure 3 displays a positive correlation between $q_{\rm AMP}$ and the reduction of the maximum PNS temperature reached in the course of the evolution (with respect to the reference model). We find that the dependence of explosion time and energy on $q_{\rm AMP}$ [Eq. (19)] is nonlinear. All these models (A11, A16, A20, and A23 with $q_{\rm AMP} = 0.3,\ 10^{-1},\ 3\times10^{-2},\ 10^{-2}$, respectively) produce quick and strong explosions, yet in the case of model A23 less energetic than model A4 ($q_{\rm AMP} = 1$).

We also note that the third free parameter in the AMP model, i.e., the sterile neutrino mass, $m_{\rm h}$, does not introduce a new kind of dynamics. It influences both their production rate (Table II) and lifetime [Eq. (16)]. One can vary either $m_{\rm h}$ or adequately both $\mu_{\rm h}$ and $\mu_{\rm tr}$ achieving the same effect. Indeed, models A29 ($m_{\rm h} = 50\ {\rm MeV}/c^2$, $q_{\rm AMP} = 0.2$, $\mu_{\rm tr} = 2\mu_{\rm tr}^{\rm ref}$) and A30 ($m_{\rm h} = 80\ {\rm MeV}/c^2$, $q_{\rm AMP} = 1$, $\mu_{\rm tr} = \mu_{\rm tr}^{\rm ref}$) produce essentially the same results in terms of explosion time, radius, and energy. This demonstrates that there is a degeneracy of the three-dimensional parameter space of the AMP model ($m_{\rm h}$, $\mu_{\rm h}$, $\mu_{\rm tr}$).

Finally, in the top panel of Fig. 7, we present explosion energies of all AMP models A1–A30 as a function of the magnetic, $\mu_{\rm h}$, and transition moment, $\mu_{\rm tr}$, of the sterile neutrinos. Depending on theses parameters, we obtain nonexploding models (marked with empty diamonds), or successful explosions with energies which are compatible with astrophysical observations (light gray are) or too high ($E_{\rm expl} > 2\times10^{52}$ erg; yellow area).

The FKP family of models has only two free parameters, neutrino mass, $m_{\rm h}$, and the mixing angle, $\sin^2\theta$. Both of them affect sterile neutrino production rate [see Eqs. (9)–(11)] and lifetime [Eq. (7)]. Hence, this is the first difference with respect to the AMP model, where these quantities can be tweaked independently. Compared to the AMP model with the default parameters (A4), the life time of the neutrinos in the default FKP model (F8) is long. Thus, explosions of the type found for model F8, i.e., an expulsion of the outer layers are rather common here. Furthermore, the explosions are on average weaker and occur later than in the AMP models. The higher $m_{\rm h}$, the stronger this tendency. Model F13 with $m_{\rm h} = 250\ {\rm MeV}/c^2$, and the default mixing angle (i.e., $q_{\rm FKP} = 1$) fails to explode at all, and only a higher production rate (models F14–F18) can compensate for this failure. We note that in models F15–F18 (and others with $q_{\rm FKP} \gtrsim 6$), the explosion is triggered by the standard shock revival mechanism.

In the bottom panel of Fig. 7, where we present all FKP models, we see that also some of them lead to too energetic explosions ($E_{\rm expl} > 2\times10^{52}$ erg). This means that also in the FKP model, some combinations of $m_{\rm h}$ and $\sin^2\theta$ can be excluded based on our simulation results.

We finally note that the only exploding models with $m_{\rm h} = 300\ {\rm MeV}/c^2$ are F21 and F22. However, as already mentioned in Sec. II, at such high masses, reactions like in Eq. (13) should be included. This would in turn lead to a further reduction of the sterile neutrino lifetimes, and a less efficient energy transfer because of their shorter mean free path. Consequently, models F21 and F22 would most likely fail to yield a successful explosion. Therefore, we may conclude that impact of the FKP neutrinos with $m_{\rm h} \gtrsim 300\ {\rm MeV}/c^2$ on core-collapse would be marginal.

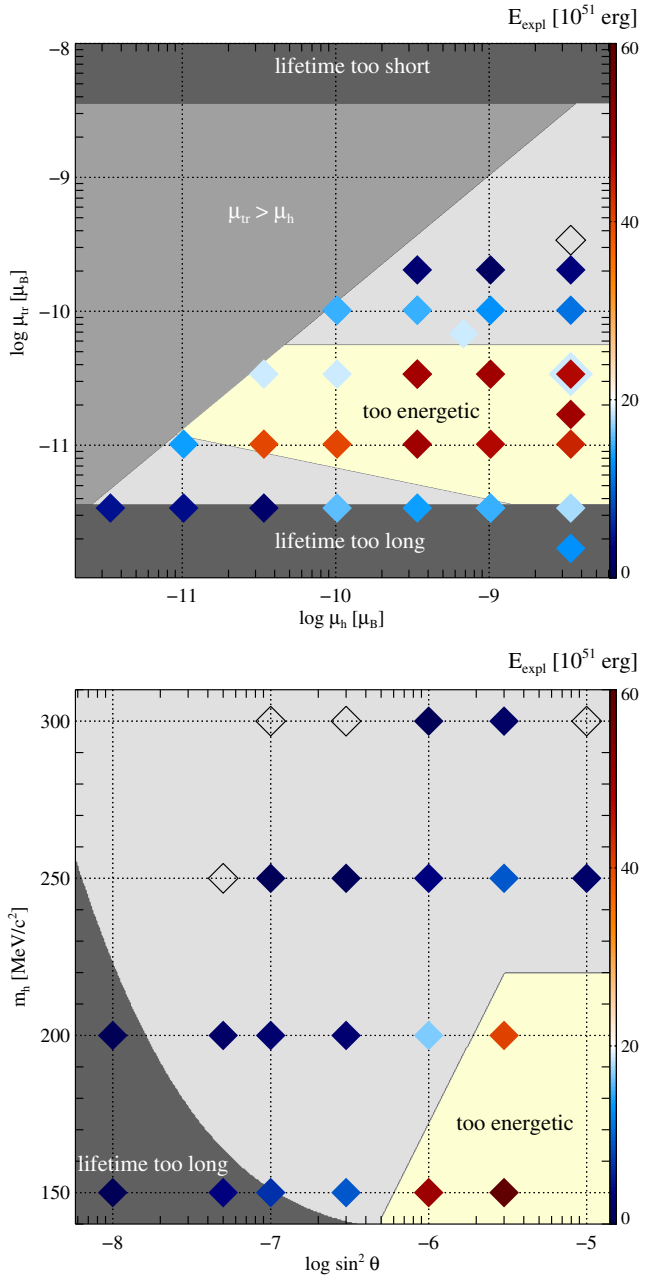

FIG. 7. Explosion energies of all AMP (top) and FKP (bottom) models as a function of, respectively, the magnetic, μ_h, and transition moment, μ_{tr} (AMP), and of mass, m_h, and mixing angle $\sin^2\theta$ (FKP) of the sterile neutrinos. In all AMP models but A30 (with $m_h = 80$ MeV$/c^2$, $m_h = 3.4 \times 10^{-9}\mu_B$, and $\mu_{tr} = 3.4 \times 10^{-11}\mu_B$), sterile neutrino mass $m_h = 50$ MeV$/c^2$. Non-exploding models are marked with empty diamonds. Regions of the parameter space with an either too long (cosmological constraint) or too short (experimental contraints) lifetime of sterile neutrinos are marked with dark gray. Light gray denotes region not excluded by our simulations. Models in yellow region are too energetic ($E_{expl} > 2 \times 10^{52}$ erg). In the gray region of $\mu_{tr} > \mu_h$ (top), the production channel $\nu X -> \nu_h X$ (not included in the AMP model nor in our code) is important relative to (or even dominant over) $e^+e^- -> \bar{\nu}_h\nu_h$ and therefore exploring it numerically was beyond the scope of this paper.

V. SUMMARY & CONCLUSIONS

We have performed one-dimensional simulations of the core collapse of a single progenitor star of $M_{ZAMS} = 15\ M_\odot$ with the two models of [29,30] for sterile neutrinos in the mass range of 50 to 300 MeV$/c^2$ that can be produced by several different channels and decay into active neutrinos and other particles of the SM. In both models, the interactions of the neutrinos depend on a few unknown free parameters (in both cases the neutrino masses, moreover, for the FKP model the mixing angle, and for AMP the magnetic moment as well as the transition moment), which we varied in order to assess their influence on the dynamics of core collapse and find potentially excluded combinations of values. The progenitor (model s15s7w2 of [50]) is known to fail producing a successful explosion in one-dimensional simulations with only active neutrinos, as we verify in our reference model to which the simulations with sterile neutrinos are compared.

We find that the AMP model [30] with the default parameters (i.e., $m_h = 50$ MeV$/c^2$, $\mu_h = \mu_h^{ref}$, and $\mu_{tr} = \mu_{tr}^{ref}$) predicts very large production rates of sterile neutrinos in core collapse. They are responsible for a very efficient energy transfer (i.e., neutrino cooling and heating) from the PNS to the postshock matter and consequently a successful explosion. In fact, the explosion energy, higher than 10^{52} erg, corresponds to the branch of hypernovae. However, hypernovae are only fairly rare among stellar core collapse, and their energies clusters at $\sim 10^{52}$ erg with an upper limit of $\sim 2 \times 10^{52}$ erg [55]. Taking all these facts together, we may exclude a large part of the parameter space for the magnetic and transition moments (see the top panel of Fig. 7), including the reference values of AMP, $\mu_h^{ref} = 3.4 \times 10^{-9}\mu_B$ and $\mu_{tr}^{ref} = 3.4 \times 10^{-11}\mu_B$, respectively.

Lowering the magnetic moment reduces the production rate of the sterile neutrinos and therefore their energy transfer efficiency and leads to less energetic explosions. Finally for $\mu_h = 10^{-2}\mu_h^{ref}$ (i.e., $q_{AMP} = 10^{-4}$), no explosion occurs.

We find that AMP sterile neutrinos with transition moments $\mu_{tr} \gtrsim 5\mu_{tr}^{ref}$ have too short lifetimes to change the dynamics of the core collapse in spherical symmetry. Due to their very short lifetime, they decay before they leave the PNS, failing to efficiently transfer the energy necessary for the shock revival. We discover that sterile neutrinos with $\mu_{tr} \lesssim 0.1\mu_{tr}^{ref}$ lead to a new type of explosions. Their long lifetimes allow them to travel through the shock and only decay and release their energy in the pre-shock matter. Such an explosion would produce an electromagnetic signal significantly differing from common events because of the relative absence of heavy elements in the ejecta.

The (much better constrained) sterile neutrino mass, $m_h = 50 - 80$ MeV$/c^2$, has a secondary impact on the

dynamics of the core collapse. Moreover, we find that there is a certain degeneracy of the three-dimensional parameter space (m_h, μ_h, μ_{tr}) of the AMP model (cf. models A29 and A30).

In the FKP model [29], explosions driven by the aforementioned new mode type, that is to say, not through shock revival, occupy a relatively large fraction of the space of model parameters compared to the AMP model, including the standard parameters (i.e., $m_h = 200$ MeV$/c^2$ and $\sin^2\theta = 5 \times 10^{-8}$). For larger values of $\sin^2\theta$, however, shock revival is more likely to occur. The maximum explosion energies can exceed 2×10^{52} erg, as for the AMP models.

We conclude that sterile neutrinos of both models can have a significant impact on the dynamics of the core collapse. In fact, for some paramers (allowed by the state of the art particle physics), they can lead to too energetic explosions (see Fig. 7). Hence, with the help of the astrophysics data and our simulations, it is possible to further constrain the parameter space of the hypothetical sterile neutrinos. We plan to perform simulations with more progenitor stars with this goal in mind.

In the spherically symmetric simulations, many (magneto)hydrodynamical phenomena like convection, the standing accretion shock instability (SASI), and the magnetohydrodynamical phenomena are suppressed. However, they are of crucial importance for CCSNe, as multidimensional models show [12,13]. They can, in particular, lead to successful supernova explosions completely without contributions from nonstandard particle physics such as sterile neutrinos (although still not matching all observational data). This fact may seemingly remove the necessity to include sterile neutrinos in supernova models. However, we argue that, besides the possibility of constraining neutrino models by simulations of core collapse, our models show that sterile neutrinos can be produced at large rates even in models where they do not cause a dramatic change in the dynamics. In such cases, though not the dominant component in the models, their influence might manifest in more indirect ways. They may affect the development of the aforementioned instabilities by, e.g., modifying the thermal stratification of the core or change the cooling of the PNS over the first few seconds after its formation. Moreover, the entropy stratification in the PNS may be significantly affected by the copious numbers of sterile neutrinos effectively carrying entropy from the PNS center to its outer layers. The most relevant consequence of such a dynamical change could be the (partial or total) damping of the convection close to the PNS surface. Since it is in principle possible to observe these convective motions through the fingerprint that leave on the gravitational wave signature (see, e.g., [57,58]), understanding the changes induced by the action of sterile neutrinos there is important. Furthermore, sterile neutrinos can act as a source of viscosity (as standard neutrinos). Thus, they may also impact the development of the magnetorotational instability (e.g., [59]). Furthermore, the production of many nuclei in supernovae is sensitive to the detailed thermodynamic conditions of the ejecta, which might allow to infer the existence and the properties of sterile neutrinos from the nucleosynthetic yields of explosions. We find it worthwhile to investigate these effects in future multidimensional simulations.

ACKNOWLEDGMENTS

M. A. A., M. O., and T. R. acknowledge support from the European Research Council (Grant No. CAMAP-259276) and from the Spanish Ministry of Economy and Competitiveness (MINECO) and the Valencian Community grants under Grants No. AYA2015-66899-C2-1-P and No. PROMETEOII/2014-069, respectively. The work of M. M. has been supported by MINECO of Spain (FPA2016-78220) and by Junta de Andalucía (FQM101). M. A. P. G. acknowledges support from Junta de Castilla y León SA083P17 and MINECO FIS2015-65140-P projects. M. A. A. and M. A. P. G. thank the PHAROS COST Action (CA16214) for partial support. M. A. A. thanks the GWverse COST Action (CA16104) for partial support. We thank Meng-Ru Wu and Tobias Fischer for valuable discussions and the anonymous referee whose useful remarks greatly improved the quality of this manuscript. The computations were performed under Grants No. AECT-2017-2-0006, No. AECT-2017-3-0007, and No. AECT-2018-1-0010 of the Spanish Supercomputing Network on the *MareNostrum* of the Barcelona Supercomputing Centre, and on the cluster *Lluisvives* of the Servei d'Informàtica of the University of Valencia.

APPENDIX A: PRODUCTION RATES IN AMP MODEL

In Table II, we provide production rates of sterile neutrinos in the AMP model with $\mu_h = \mu_h^{ref} = 3.4 \times 10^{-9}\mu_B$ and the lower ($m_h = 50$ MeV$/c^2$) and upper ($m_h = 80$ MeV$/c^2$) limit for their mass. These tabulated values are more precise than the original fit deduced in Eq. (24) of [30].

TABLE II. Production rates Q_{50} and Q_{80} [erg cm^{-3} s^{-1} of AMP sterile neutrinos with masses $m_h = 50$ and $m_h = 80$ MeV$/c^2$, respectively, as a function of temperature T[MeV$/k_B$] and chemical potential of electrons μ_e[MeV].

T	μ_e	Q_{50}	Q_{80}
5	20	1.53656×10^{26}	5.66121×10^{21}
5	40	1.36192×10^{26}	5.65149×10^{21}
5	60	6.62017×10^{25}	5.38001×10^{21}
5	80	1.40457×10^{25}	3.70775×10^{21}
5	100	1.57973×10^{24}	1.36088×10^{21}

(Table continued)

TABLE II. *(Continued)*

T	μ_e	Q_{50}	Q_{80}
5	120	1.14701×10^{23}	2.67659×10^{20}
5	140	5.92976×10^{21}	3.23395×10^{19}
10	20	3.35603×10^{31}	4.6994×10^{29}
10	40	2.93381×10^{31}	4.61384×10^{29}
10	60	2.0258×10^{31}	4.23021×10^{29}
10	80	1.05091×10^{31}	3.28535×10^{29}
10	100	4.24676×10^{30}	2.01978×10^{29}
10	120	1.41374×10^{30}	9.8191×10^{28}
10	140	4.06273×10^{29}	3.90146×10^{28}
15	20	3.87518×10^{33}	3.77445×10^{32}
15	40	3.45646×10^{33}	3.65218×10^{32}
15	60	2.72116×10^{33}	3.33863×10^{32}
15	80	1.85546×10^{33}	2.76958×10^{32}
15	100	1.10604×10^{33}	2.03238×10^{32}
15	120	5.88587×10^{32}	1.3159×10^{32}
15	140	2.85587×10^{32}	7.60523×10^{31}
20	20	5.91745×10^{34}	1.46498×10^{34}
20	40	5.40009×10^{34}	1.40987×10^{34}
20	60	4.55643×10^{34}	1.29812×10^{34}
20	80	3.52661×10^{34}	1.12208×10^{34}
20	100	2.51089×10^{34}	8.99522×10^{33}
20	120	1.65963×10^{34}	6.67171×10^{33}
20	140	1.02932×10^{34}	4.59968×10^{33}
25	20	3.81804×10^{35}	1.60404×10^{35}
25	40	3.55223×10^{35}	1.54426×10^{35}
25	60	3.12922×10^{35}	1.43561×10^{35}
25	80	2.60148×10^{35}	1.27651×10^{35}
25	100	2.04338×10^{35}	1.07861×10^{35}
25	120	1.52328×10^{35}	8.64511×10^{34}
25	140	1.0841×10^{35}	6.58566×10^{34}
30	20	1.56005×10^{36}	9.09296×10^{35}
30	40	1.47347×10^{36}	8.78013×10^{35}
30	60	1.33639×10^{36}	8.24119×10^{35}
30	80	1.1624×10^{36}	7.48168×10^{35}
30	100	9.70326×10^{35}	6.54588×10^{35}
30	120	7.79272×10^{35}	5.51251×10^{35}
30	140	6.04193×10^{35}	4.47226×10^{35}
35	20	4.83426×10^{36}	3.48875×10^{36}
35	40	4.61865×10^{36}	3.38157×10^{36}
35	60	4.27645×10^{36}	3.2018×10^{36}
35	80	3.8358×10^{36}	2.95345×10^{36}
35	100	3.33478×10^{36}	2.64876×10^{36}
35	120	2.81431×10^{36}	2.30773×10^{36}
35	140	2.31051×10^{36}	1.95406×10^{36}
40	20	1.2473×10^{37}	1.03957×10^{37}
40	40	1.20209×10^{37}	1.01149×10^{37}
40	60	1.12999×10^{37}	9.65008×10^{36}
40	80	1.03601×10^{37}	9.01421×10^{36}
40	100	9.26821×10^{36}	8.23478×10^{36}
40	120	8.09845×10^{36}	7.35349×10^{36}
40	140	6.92149×10^{36}	6.42031×10^{36}
45	20	2.82713×10^{37}	2.60171×10^{37}
45	40	2.74285×10^{37}	2.54028×10^{37}
45	60	2.60775×10^{37}	2.43927×10^{37}
45	80	2.42982×10^{37}	2.30165×10^{37}
45	100	2.21964×10^{37}	2.13277×10^{37}
45	120	1.98928×10^{37}	1.94022×10^{37}
45	140	1.7508×10^{37}	1.73315×10^{37}

APPENDIX B: OPACITIES

Absorption opacities of the sterile neutrinos in the FKP and the AMP models, respectively, are

$$\kappa_{\rm a} = \frac{1}{\gamma_{\rm h}\beta_{\rm h}\tau_{\rm h}c} \tag{B1}$$

and

$$\kappa_{\rm a} = \left[\frac{1}{\gamma_{\rm h}\beta_{\rm h}\tau_{\rm h}c} + (0.9n_p + 2.1n_e)10^{-45}\right]\left(\frac{\mu_{\rm tr}}{\mu_{\rm tr}^{\rm ref}}\right)^2, \tag{B2}$$

with $\tau_{\rm h}$ given by Eqs. (16) and (7), respectively. Hence, in both models, they depend on the Lorentz factor, $\gamma_{\rm h}$, of the sterile neutrino.

In the FKP model, combining Eqs. (2)–(4) from [29], we find that on average,

$$\gamma_{\rm h} \approx 1.3\left(\frac{Tk_{\rm B}}{35\ {\rm MeV}}\right)^{0.4}\left(\frac{200\ {\rm MeV}}{m_{\rm h}c^2}\right). \tag{B3}$$

In the AMP model, we calculated the energy distribution of the sterile neutrinos as a function of temperature and found that they are produced with an average Lorentz factor

$$\gamma_{\rm h} \approx 0.93 + 2.6\frac{Tk_{\rm B}}{m_{\rm h}c^2}. \tag{B4}$$

Hence, at $Tk_B < 50$ MeV, the neutrinos are in both models mildly relativistic. Therefore, as a first approximation, in our calculation of the opacities of sterile neutrinos, we put $\gamma_{\rm h}\beta_{\rm h} \approx 1$ and neglected their increased lifetimes. In other words, we used Eqs. (32) and (29), instead of Eqs. (B1) and (B2), respectively.

[1] G. Mention, M. Fechner, T. Lasserre, T. A. Mueller, D. Lhuillier, M. Cribier, and A. Letourneau, Phys. Rev. D **83**, 073006 (2011).
[2] C. Giunti and M. Laveder, Phys. Rev. C **83**, 065504 (2011).
[3] C. Athanassopoulos *et al.* (LSND Collaboration), Phys. Rev. Lett. **81**, 1774 (1998).
[4] A. A. Aguilar-Arevalo *et al.* (MiniBooNE Collaboration), Phys. Rev. Lett. **102**, 101802 (2009).
[5] A. A. Aguilar-Arevalo *et al.* (MiniBooNE Collaboration), arXiv:1805.12028.
[6] G. Magill, R. Plestid, M. Pospelov, and Y.-D. Tsai, arXiv:1803.03262.
[7] G. G. Raffelt and S. Zhou, Phys. Rev. D **83**, 093014 (2011).
[8] M. Á. Pérez-García and J. Silk, Phys. Lett. B **744**, 13 (2015).
[9] M. Cermeño, M. Á. Pérez-García, and J. Silk, Pub. Astron. Soc. Aust. **34**, e043 (2017).
[10] K. Abazajian, G. M. Fuller, and M. Patel, Phys. Rev. D **64**, 023501 (2001).
[11] S. Hannestad and G. G. Raffelt, Phys. Rev. Lett. **87**, 051301 (2001).
[12] H.-T. Janka, T. Melson, and A. Summa, Annu. Rev. Nucl. Part. Sci. **66**, 341 (2016).
[13] H.-T. Janka, in *Handbook of Supernovae*, edited by A. W. Alsabti and P. Murdin (Springer, New York, 2017), p. 1095.
[14] P. Mösta, S. Richers, C. D. Ott, R. Haas, A. L. Piro, K. Boydstun, E. Abdikamalov, C. Reisswig, and E. Schnetter, Astrophys, J. Lett. **785**, L29 (2014).
[15] M. Obergaulinger and M. Á. Aloy, Mon. Not. R. Astron. Soc. **469**, L43 (2017).
[16] R. Bollig, H.-T. Janka, A. Lohs, G. Martínez-Pinedo, C. J. Horowitz, and T. Melson, Phys. Rev. Lett. **119**, 242702 (2017).
[17] A. Mirizzi, I. Tamborra, H.-T. Janka, N. Saviano, K. Scholberg, R. Bollig, L. Hüdepohl, and S. Chakraborty, Nuovo Cimento Riv. Ser. **39**, 1 (2016).
[18] T. Fischer, I. Sagert, G. Pagliara, M. Hempel, J. Schaffner-Bielich, T. Rauscher, F.-K. Thielemann, R. Käppeli, G. Martínez-Pinedo, and M. Liebendörfer, Astrophys. J. Suppl. Ser. **194**, 39 (2011).
[19] B. Pontecorvo, Zh. Eksp. Teor. Fiz. **53**, 1717 (1967) [Sov. Phys. JETP **26**, 984 (1968)].
[20] A. Kusenko and G. Segrè, Phys. Rev. Lett. **79**, 2751 (1997).
[21] A. Wongwathanarat, H.-T. Janka, and E. Müller, Astron. Astrophys. **552**, A126 (2013).
[22] K. A. Olive and M. S. Turner, Phys. Rev. D **25**, 213 (1982).
[23] S. Dodelson and L. M. Widrow, Phys. Rev. Lett. **72**, 17 (1994).
[24] R. A. Malaney, G. D. Starkman, and L. Widrow, Phys. Rev. D **52**, 5480 (1995).
[25] S. Colombi, S. Dodelson, and L. M. Widrow, Astrophys. J. **458**, 1 (1996).
[26] K. N. Abazajian, Phys. Rev. Lett. **112**, 161303 (2014).
[27] A. Boyarsky, O. Ruchayskiy, D. Iakubovskyi, and J. Franse, Phys. Rev. Lett. **113**, 251301 (2014).
[28] E. Bulbul, M. Markevitch, A. Foster, R. K. Smith, M. Loewenstein, and S. W. Randall, Astrophys. J. **789**, 13 (2014).
[29] G. M. Fuller, A. Kusenko, and K. Petraki, Phys. Lett. B **670**, 281 (2009).
[30] C. Albertus, M. Masip, and M. A. Pérez-García, Phys. Lett. B **751**, 209 (2015).
[31] M.-R. Wu, T. Fischer, L. Huther, G. Martínez-Pinedo, and Y.-Z. Qian, Phys. Rev. D **89**, 061303 (2014).
[32] M. Obergaulinger, Ph.D. thesis, Technische Universität München, 2008.
[33] O. Just, M. Obergaulinger, and H.-T. Janka, Mon. Not. R. Astron. Soc. **453**, 3386 (2015).
[34] A. Bueno, M. Masip, P. Sánchez-Lucas, and N. Setzer, Phys. Rev. D **88**, 073010 (2013).
[35] S. N. Gninenko, Phys. Rev. D **83**, 015015 (2011).
[36] A. D. Dolgov, S. H. Hansen, G. Raffelt, and D. V. Semikoz, Nucl. Phys. **B590**, 562 (2000).
[37] D. I. Britton, S. Ahmad, D. A. Bryman, R. A. Burnham, E. T. H. Clifford, P. Kitching, Y. Kuno, J. A. Macdonald, T. Numao, A. Olin, J. M. Poutissou, and M. S. Dixit, Phys. Rev. D **46**, R885 (1992).
[38] A. V. Artamonov and Anonymous (E949 Collaboration), Phys. Rev. D **91**, 059903 (2015).
[39] E. C. Gil *et al.* (NA62 Collaboration), Phys. Lett. B **778**, 137 (2018).
[40] J. Orloff, A. Rozanov, and C. Santoni, Phys. Lett. B **550**, 8 (2002).
[41] M. Masip, P. Masjuan, and D. Meloni, J. High Energy Phys. 01 (2013) 106.
[42] A. Bartl, R. Bollig, H.-T. Janka, and A. Schwenk, Phys. Rev. D **94**, 083009 (2016).
[43] M. Obergaulinger and M. Á. Aloy, J. Phys. Conf. Ser. **932**, 012043 (2017).
[44] T. Rembiasz, M. Obergaulinger, P. Cerdá-Durán, M.-Á. Aloy, and E. Müller, Astrophys. J. Suppl. Ser. **230**, 18 (2017).
[45] A. Suresh and H. Huynh, J. Comput. Phys. **136**, 83 (1997).
[46] A. Harten, P. D. Lax, and B. V. Leer, SIAM Rev. **25**, 35 (1983).
[47] J. M. Lattimer and F. D. Swesty, Nucl. Phys. **A535**, 331 (1991).
[48] A. Marek, H. Dimmelmeier, H.-T. Janka, E. Müller, and R. Buras, Astron. Astrophys. **445**, 273 (2006).
[49] E. Endeve, C. Y. Cardall, and A. Mezzacappa, arXiv: 1212.4064.
[50] S. E. Woosley and T. A. Weaver, Astrophys. J. Suppl. Ser. **101**, 181 (1995).
[51] M. Obergaulinger, H.-T. Janka, and M. A. Aloy, Mon. Not. R. Astron. Soc. **445**, 3169 (2014).
[52] M. Obergaulinger, O. Just, H.-T. Janka, M. A. Aloy, and C. Aloy, in *Proceedings of the 8th International Conference of Numerical Modeling of Space Plasma Flows (ASTRONUM 2013)*, edited by N. V. Pogorelov, E. Audit, and G. P. Zank, Astronomical Society of the Pacific Conference Series, Vol. 488 (Astronomical Society of the Pacific, 2014), p. 255.
[53] M. Obergaulinger, O. Just, and M. Á. Aloy, J. Phys. G **45**, 084001 (2018).
[54] K. Nomoto, M. Tanaka, N. Tominaga, and K. Maeda, New Astron. Rev. **54**, 191 (2010).

[55] P. A. Mazzali, A. I. McFadyen, S. E. Woosley, E. Pian, and M. Tanaka, Mon. Not. R. Astron. Soc. **443**, 67 (2014).
[56] S. Dong *et al.*, Science **351**, 257 (2016).
[57] P. Cerdá-Durán, N. DeBrye, M. A. Aloy, J. A. Font, and M. Obergaulinger, Astrophys. J. Lett. **779**, L18 (2013).
[58] H. Andresen, B. Müller, E. Müller, and H.-T. Janka, Mon. Not. R. Astron. Soc. **468**, 2032 (2017).
[59] J. Guilet, E. Müller, and H.-T. Janka, Mon. Not. R. Astron. Soc. **447**, 3992 (2015).